

Revealing an origin of temperature-dependent structural change in intrinsically disordered proteins

Rintaro Inoue,¹ Takashi Oda,² Hiroshi Nakagawa,^{2,3} Taiki Tominaga,⁴ Takahisa Ikegami,⁵ Tsuyoshi Konuma,⁵ Hiroki Iwase,⁴ Yukinobu Kawakita,² Mamoru Sato,^{5,6,*} and Masaaki Sugiyama^{1,*}

¹Institute for Integrated Radiation and Nuclear Science, Kyoto University, Osaka, Japan; ²J-PARC Center, JAEA, Ibaraki, Japan; ³Materials Sciences Research Center, JAEA, Ibaraki, Japan; ⁴Neutron Science and Technology Center, Comprehensive Research Organization for Science and Society (CROSS), Ibaraki, Japan; ⁵Graduate School of Medical Life Science, Yokohama City University, Yokohama, Japan; and ⁶Neutron Industrial Application Promotion Center, Comprehensive Research Organization for Science and Society (CROSS), Ibaraki, Japan

ABSTRACT Intrinsically disordered proteins (IDPs) show structural changes stimulated by changes in external conditions. This study aims to reveal the temperature dependence of the structure and the dynamics of the intrinsically disordered region of the helicase-associated endonuclease for fork-structured DNA, one of the typical IDPs, using an integrative approach. Small-angle X-ray scattering (SAXS) and circular dichroism (CD) studies revealed that the radius of gyration and ellipticity at 222 nm remained constant up to 313–323 K, followed by a decline above this temperature range. NMR studies revealed the absence of a promotion of the α helix. As a result, SAXS, CD, and NMR data strongly suggest that these temperature-dependent structural changes were primarily due to a reduction in the content of the polyproline II (PPII) helix. Moreover, quasielastic neutron scattering studies revealed a slight change in the activation energy in a similar temperature range. Considering the concept of glass transition, it is posited that dynamical cooperativity between the PPII helix and water may play a significant role in these structural changes. The findings suggest that internal dynamics are crucial for regulating the structure of IDPs, highlighting the importance of considering dynamical cooperativity in future studies of protein behavior under varying temperature conditions.

SIGNIFICANCE The structural response of intrinsically disordered proteins (IDPs) to changes in the solution environment differs distinctly from that of folded globular proteins (FGPs). Although the FGP increases in size with increasing temperature, the IDP decreases in size. We investigated the temperature-dependent structural and dynamic behaviors of the intrinsically disordered region of the helicase-associated endonuclease for fork-structured DNA as an example of an IDP. We observed not only changes in the secondary and tertiary structures with increasing temperature but also an acceleration of the internal dynamics. The transition temperature at which both structural and dynamic changes were observed was 313–323 K. It was concluded that the dynamical cooperativity between the polyproline II helix and water plays a significant role in temperature-dependent structural behaviors.

INTRODUCTION

Proteins that lack an ordered structure (1) are categorized as intrinsically disordered proteins (IDPs). IDPs are distinguished by the prevalence of highly charged residues,

whereas folded globular proteins (FGPs) are characterized by a hydrophobic interior and hydrophilic exterior (2). The discrepancy in the residue composition between IDPs and FGPs could cause disparate structural responses to alterations in the solution environment. Consequently, we focused on how IDPs and FGPs respond to temperature changes as a case study of environmental variation. The IDP undergoes a reduction in size with an increase in temperature (3–5), whereas the FGP exhibits an increase in size. Although computational approaches have been employed to elucidate the mechanism underlying the reduction in size observed with increasing temperature in IDPs (6,7), a

Submitted August 10, 2024, and accepted for publication December 20, 2024.

*Correspondence: m_sato23@cross.or.jp or sugiyama.masaaki.5n@kyoto-u.ac.jp

Rintaro Inoue and Takashi Oda contributed equally to this work.

Editor: Frank Gabel.

<https://doi.org/10.1016/j.bpj.2024.12.022>

© 2025 The Authors. Published by Elsevier Inc. on behalf of Biophysical Society.

This is an open access article under the CC BY-NC-ND license (<http://creativecommons.org/licenses/by-nc-nd/4.0/>).

definitive conclusion remains elusive. Further experimental investigations are necessary to improve our understanding of this unique phenomenon.

Given that IDPs possess highly flexible structures regulated by internal dynamics (7), it is crucial to investigate their structural and dynamic properties to elucidate the underlying mechanisms of their temperature-dependent structural changes. Experimental techniques capable of detecting structures ranging from the local to higher-order scale can offer key insights into temperature-dependent structural changes in IDPs (2). Lin et al. succeeded in revealing the structure of a highly flexible protein through small-angle X-ray scattering (SAXS), NMR, and molecular simulation (8), demonstrating the significance of complementary uses of various experimental techniques for the study of a flexible protein. Accordingly, a combination of SAXS/small-angle neutron scattering (SANS), circular dichroism (CD), and NMR was employed to investigate the structural characteristics of the IDP at various temperatures. Moreover, the temperature dependence of the internal dynamics of the IDP, ranging from subnanoseconds to microseconds, has been directly studied using quasielastic neutron scattering (QENS) (7,9–12).

In this study, the intrinsically disordered region (IDR) of the helicase-associated endonuclease for fork-structured DNA (Hef-IDR) was selected as an example of an IDP. The Hef from *Thermococcus kodakaraensis*, a hyperthermophilic archaeon (13) (UniProt: Q5JJ98), is composed of an N-terminal helicase domain (residues 1–492), a C-terminal nuclease domain (residues 594–811), and an IDR (residues 493–593) intervening in the two globular domains. The main function of Hef is to repair damaged DNA. Specifically, the helicase and nuclease domains unwind and cleave fork-structured DNA, respectively. In contrast, the IDR interacts with multiple proteins involved in DNA repair and replication. The objective of this study was to elucidate the mechanism of temperature-dependent structural changes in IDPs through integrative analyses obtained by combining the aforementioned techniques.

MATERIALS AND METHODS

Samples

Hef-IDR was produced in *Escherichia coli* BL21 CodonPlus (DE3)-RIL cells (Agilent). The pET28a plasmid (Novagen) harboring the Hef-IDR gene fragment was modified from that reported previously (13) to remove the histidine tag and TEV protease recognition sequence. The *E. coli* cells were grown at 310 K in Luria Broth (LB) medium. When the *E. coli* culture reached an optical density at 660 nm of 0.5, expression of Hef-IDR expression was induced by adding isopropyl beta-D-thiogalactopyranoside to 1 mM. After cultivation at 298 K for 18 h, the cells were harvested by centrifugation, and the cell lysate was prepared by sonication in buffer A (50 mM Tris [pH 8.0], 0.5 M NaCl, 0.5 mM EDTA, and 1 mM phenylmethylsulfonyl fluoride). After centrifugation for 20 min at $20,000 \times g$, the supernatant was heated at 353 K for 20 min. The heat-resistant fraction was diluted with buffer B (20 mM Tris-HCl [pH 8.0] and 0.5 mM EDTA) and then applied to a cation exchange column (HiTrap SP HP, Cytiva), which

was developed with a linear gradient of 0.05–0.6 M NaCl. The eluted fractions were applied to a gel-filtration column (HiLoad 26/600 Superdex200, Cytiva) which was equilibrated with buffer C (10 mM HEPES-NaOH [pH 7.5], 350 mM NaCl, and 0.1 mM EDTA). To inactivate contaminating proteases, purified Hef-IDR was heated to 353 K for 10 min, rapidly cooled in liquid nitrogen, and stored at 193 K.

SAXS

The SAXS measurements were conducted using a Photon Factory BL-6A instrument (Tsukuba, Japan). The X-ray wavelength and the sample-to-camera distance were set to 1.5 Å and 2038.9 mm, respectively. PILATUS 1M was used as the detector, and the accessible Q range was from 0.0085 to 0.27 \AA^{-1} . The data acquisition time and number of acquisitions were 2 s and 200, respectively. Prior to data reduction, we checked the radius of gyration (R_g) as a function of the frame, and no change in R_g was observed. We then averaged all 200 frames to obtain the scattering profile. To minimize the risk of radiation damage, the Hef-IDR solution at a concentration of 12 mg/mL was prepared in a buffer (10 mM HEPES [pH 7.5], 100 mM NaCl, 0.1 mM EDTA) containing 10 mM Tris (2-carboxyethyl) phosphine hydrochloride. A borosilicate capillary with an internal diameter of 2 mm and a wall thickness of 10 μm was employed for the SAXS measurements. After reaching the target temperature, the samples were incubated at this temperature for 5 min. Then, SAXS measurements were commenced after checking for the absence of bubbles in the sample capillary. The observed SAXS intensity was corrected for background, empty capillary, and buffer scattering and then transmitted and converted to absolute intensity using water as a reference. All data were analyzed using the SAngler software program (14). Data were subsequently analyzed using the ATSAS package (15,16).

SANS

The SANS experiments were conducted at the Japan Proton Accelerator Complex (Tokai, Japan) using TAIKAN (17) and at the Institute for Solid State Physics, University of Tokyo, using SANS-U (18). Concerning the instrumental setup of TAIKAN, we used wavelengths covering from 0.7 to 7.6 Å, a sample-to-detector distance of 5.6 m, and a Q resolution of $\sim 5\%$. In this study, we especially used data acquired from the small-angle bank detector of TAIKAN. ^3He liner position sensitive detectors, which were supplied by Toshiba Electron Tubes & Devices, were used, and the accessible Q range with the small-angle bank detector of TAIKAN ranged from 0.0087 to 0.5 \AA^{-1} . The data acquisition time and number of acquisitions were set to 1.5 h and 1, respectively, and the protein concentration was set to 5 mg/mL. To avoid bubbling at high temperatures, both the protein and buffer solutions were degassed at 298 K for 10 min. For the SANS experiment with SANS-U, we used the wavelength of 7 Å, sample-to-detector distances of 4 and 1.03 m, and a Q resolution of $\sim 12\%$, respectively. A two-dimensional area detector using a multiwired PSPC (model 2660N, ORDELA, USA) was used, and the accessible Q range was from 0.01 to 0.25 \AA^{-1} . The data acquisition time and a number of acquisitions were set as 1 h and 3, respectively. The protein concentration was 5 mg/mL. In both SANS measurements, a cylindrical cell with an outer diameter of 22 mm, an inner diameter of 18 mm, and an optical path of 2.0 mm was used. The measured intensity was corrected for the background, empty cell, buffer solution scattering, and transmittance. The SANS profiles were converted to absolute intensities (cm^{-1}) using standard samples or the direct beam method.

CD

The CD spectra were obtained using a Jasco J-720W spectropolarimeter. A solution of 40 μM Hef-IDR in a buffer solution comprising 10 mM HEPES

(pH 7.5), 100 mM NaCl, and 0.1 mM EDTA was analyzed. An acquisition interval of 1 nm, five acquisitions, and a scan rate of 50 nm/min were used for this measurement. After incubating at the target temperature for 5 min and checking for the absence of bubbles in the quartz cell with an optical path of 1 mm, we commenced the CD measurement at the target temperature.

NMR

Two-dimensional NMR experiment correlates amide ^{15}N atoms of a residue (i) with ^{13}C C' of residues (i) and (i-1) (CON) and NMR experiment correlates amide ^{13}C atoms of C=O in a residue (i) with ^{13}C of C-alpha atom in residues (i) and (i-1) (CACO) spectra (19) were acquired at 298, 313, and 349 K using a Bruker BioSpin Avance III HD spectrometer equipped with a TCI triple-resonance cryogenic probe with a ^1H resonance frequency of 950.15 MHz. The protein concentration of 5 mg/mL was used. The carrier frequencies were positioned at 175.6, 56.6, 120, and 4.7 ppm for the $^{13}\text{C}'$, $^{13}\text{C}\alpha$, ^{15}N , and ^1H spins, respectively. The spectral widths were set to 40 ppm (1024 data points) for the $^{13}\text{C}'$ direct dimension, 24 ppm (128 data points) for the ^{15}N indirect dimension, and 30 ppm (100 data points) for the $^{13}\text{C}\alpha$ indirect dimension. Each free induction decay comprised 128 and 160 scans for the CON and CACO experiments, respectively. Selective inversion of the $^{13}\text{C}\alpha$ spins was achieved with a 500- μs -long Q3 SURBOP pulse (20) in the context of the CACO experiment. Furthermore, the $^{13}\text{C}\alpha$ and $^{13}\text{C}'$ spins were inverted, with a 500- μs -long chirp pulse (80 kHz sweep and 20% smoothing) for the CON experiment. The remaining ^{13}C pulses were applied with a 162- μs -long Q3 cascade for 90° excitation and a 259- μs -long G4 cascade for 180° reversion. The pulses for ^1H and ^{15}N decoupling were applied using the WALTZ65 and GARP4 schemes, with radio frequency powers of 4545 and 1136 Hz, respectively. The two experiments used the in-phase/anti-phase scheme for virtual decoupling of C α -C' scalar coupling (21). Indirect dimensions were sampled using the state-time proportional phase increment (TPPI) method. An interscan delay of 1.5 s was implemented. The remaining parameters were set in accordance with the specifications outlined in Bruker pulse programs (c_con_iasq and c_caco_ia). The NMR spectra were processed using Topspin 3.6 and subsequently analyzed using POKY (22).

QENS measurements

QENS measurements were performed using an inverted-geometry time-of-flight spectrometer (BL02 DNA) (23) installed at the Materials and Life Science Experimental Facility of J-PARC, Tokai, Japan. The magnitude of the scattering vector, Q ($Q = 4\pi\sin\theta/\lambda_f$, where 2θ and $\lambda_f = 6.32 \text{ \AA}$ are the scattering angle and wavelength of the analyzed neutron, respectively), ranged from 0.12 to 1.78 \AA^{-1} , corresponding to the spatial scale from 3.5 to 31 \AA . Each sample was placed in a double-cylindrical aluminum (Al) cell (outer diameter: 14 mm; inner diameter: 13 mm; height: 45 mm) under a helium atmosphere. The resolution function was determined from vanadium measurements at 298 K, and the energy resolution (δE) was calculated to be 12 μeV , covering the timescale from 5 to 200 ps. Hef-IDR solutions (8.0 mg/mL) were analyzed at 283, 298, 323, 343, and 363 K. To avoid chemical interactions between the surface of the Al cell and the Hef-IDR solution, the Al cells used in this study were boehmite coated with D_2O . Subsequently, a Hef-IDR solution was loaded into boehmite-coated Al cells (24,25).

RESULTS

Temperature dependence of ternary and secondary structures of Hef-IDR

Fig. 1 *a* shows the SAXS profiles of the Hef-IDR at 283, 298, 323, 343, and 363 K. Using the Guinier approximation (26) (Eq. 1), the R_g was calculated using the SAXS profiles.

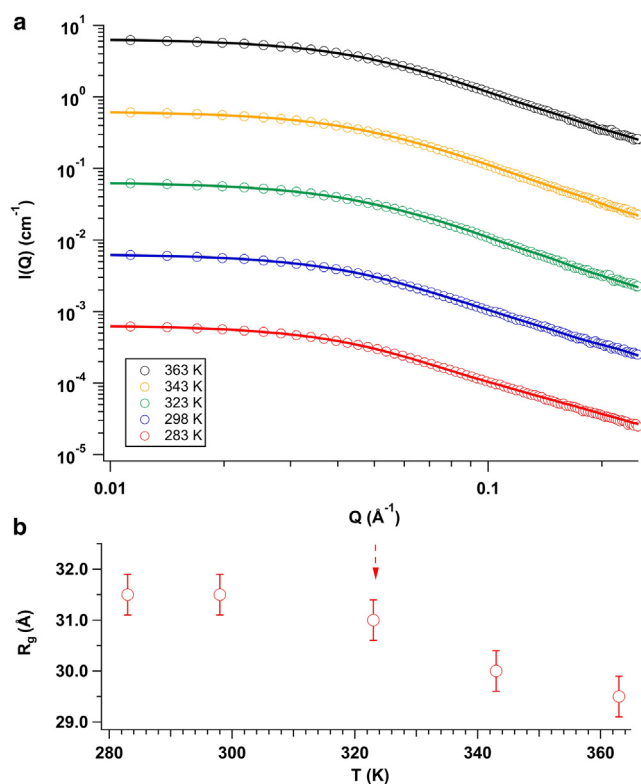


FIGURE 1 (a) SAXS profiles at 283 (red circle), 298 (blue circle), 323 (green circle), 343 (yellow circle), and 363 K (black circles), respectively. The red, blue, green, yellow, and black lines correspond to ensemble-averaged profiles. (b) Temperature dependence of R_g calculated from SAXS profiles. The solid lines are results of fits with a linear function within the temperature range of 283–323 K, and the dashed arrow corresponds to T_{tra} .

$$I(Q) = I(0)\exp\left(-R_g^2Q^2/3\right) \quad (1)$$

where $I(Q)$ and $I(0)$ correspond to the scattering intensity as a function of Q and forward scattering intensity, respectively. The results of fitting with the Guinier approximation and residual plots are summarized in Fig. S1. As shown in Fig. 1 *b*, the variation of R_g against the temperature was flat up to 323 K, and a decrease in the R_g value was observed in the temperature range above ~ 323 K. Although the detailed temperature dependence of R_g was unclear only from the SANS results owing to large error bars, at least a tendency for a reduction in R_g was observed with increasing temperature (Figs. S2 and S3). In the case of unfolding of FGPs by an increment of temperature, the collapse of secondary structures such as the α helix and β sheet occurs, leading to an increment of R_g with increasing temperature (27). This process is normally irreversible in FGPs, whereas heat-induced structural changes are reversible in IDPs (3). Hence, it is expected that stable secondary structures are not related to the temperature-dependent structural change of IDP.

To investigate the temperature dependence of the secondary structure, CD measurements were also performed on the Hef-IDR solutions at different temperatures. As shown in Fig. 2 *a*, only a broad band at 222 nm was observed in the CD spectra. Therefore, we focused on the temperature dependence of ellipticity at 222 nm ($\theta_{222\text{nm}}$). The variation of the $\theta_{222\text{nm}}$ value against temperature was almost flat up to 313 K, whereas a reduction of the $\theta_{222\text{nm}}$ value was observed in the temperature range above 313 K. (Fig. 2 *b*). The transition temperature (T_{tra}), which ranged from 313 to 323 K, was observed in the SAXS and CD measurements. Structural changes in other IDPs have been observed in similar temperature ranges (2).

Two possibilities are related to the interpretation of the temperature-dependent change of CD spectra. One is an increment of α helix with increasing temperature, and another is a decrease in the polyproline II (PPII) helix content. Following an approach reported by Trevino et al. (28), we focused on the temperature dependence of $\theta_{222\text{nm}}$ subtracted from that at 277 K ($\Delta\theta_{222\text{nm}}$). We then performed a linear fit to the temperature dependence of $\Delta\theta_{222\text{nm}}$. The resulting coefficient of determination value is 0.956. If a

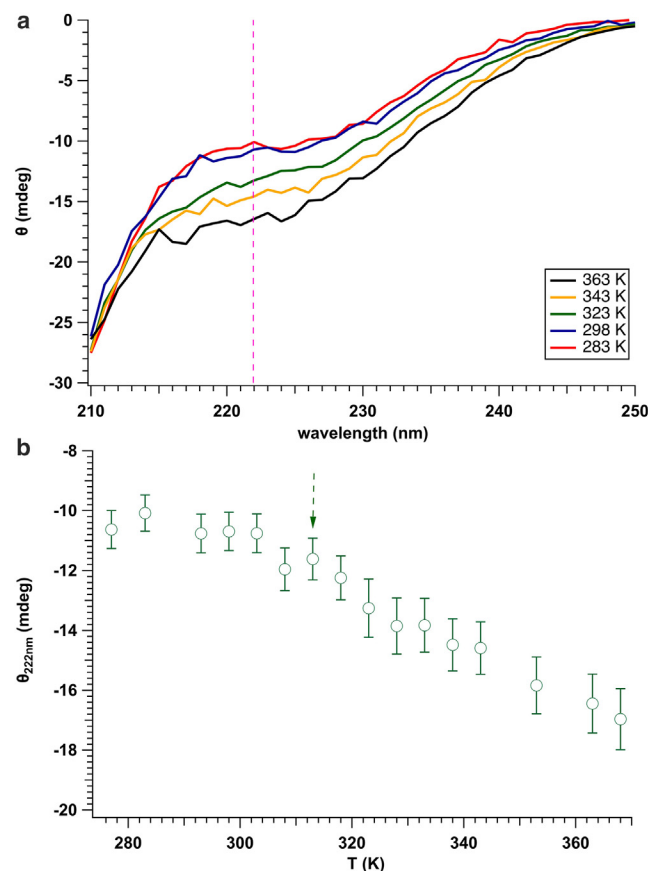


FIGURE 2 (a) CD spectra at 283 (red line), 298 (blue line), 323 (green line), 343 (yellow line), and 363 K (black line). The pink dashed line corresponds to 222 nm wavelength. (b) Temperature dependence of $\theta_{222\text{nm}}$, and the dashed arrow corresponds to T_{tra} .

stable secondary structure, such as an α helix, is formed, then a sigmoidal shape would be observable for the temperature dependence of $\Delta\theta_{222\text{nm}}$. Hence, the CD results supported the lack of a stable secondary structure in the examined temperature range (28).

To extract other structural parameters from the SAXS profile, we analyzed the SAXS profiles using Eq. 2:

$$\frac{I(Q)}{I(0)} = \frac{2}{x^2}(x - 1 + e^{-x}) + \frac{b}{L} \left[\frac{4}{15} + \frac{7}{15x} - \left(\frac{11}{15} + \frac{7}{15x} \right) e^{-x} \right] \quad (2)$$

with $x = Q^2 L b / 6$, where b and L correspond to the Kuhn length and contour length, respectively. For fitting with Eq. 2, we use the Q region, which satisfies the condition of $Q < 3/b$. The fits with Eq. 2 are shown in Fig. S4 *a*. The temperature dependence of L is shown in Fig. S4 *b*. Although the detailed temperature dependence of L was unclear due to relatively large error bars, the mean value of L ($=302 \pm 12 \text{ \AA}$) was shorter than the value expected for a random coil (362.7 \AA), and this finding is also reported for other IDPs (29). Moreover, R_g values from SAXS measurements were higher than one expected from the random coil (28.3 \AA) (30). As an alternative approach, we calculated the D_{max} values, and the results are summarized in Table S1. Reflecting the reduction in R_g with increasing temperature, the D_{max} value also decreased with increasing temperature. D_{max} values of IB5 ($N = \sim 70$, where N corresponds to a residue number) and II-I ($N = \sim 140$), which possess a PPII helix, are reported to be 110 ± 10 and $155 \pm 10 \text{ \AA}$, respectively (30). As the N value of Hef-IDR is 101, our evaluated D_{max} values are in between the two above-described two values. If the promotion of the α helix occurred with increasing temperature, then we could observe a plateau at high QR_g . As shown in Fig. S5, we could not observe a plateau even at the highest temperature. This implies that Hef-IDR is still locally rigid and elongated even at high temperatures. Hence, the L , R_g , and D_{max} values support the existence of the PPII helix in Hef-IDR. Moreover, we focused on an additional parameter. If the promotion of the α helix occurred with increasing temperature, then an increment of persistence length (l_p) due to an increment of chain rigidity would be observed. However, if loss of the PPII helix occurred with increasing temperature, then a reduction in l_p would be observed. As shown in Fig. S4 *b*, a reduction in l_p with increasing temperature was observed, reinforcing the idea of the loss of the PPII helix with increasing temperature.

To investigate the temperature dependence of the secondary structure of the Hef-IDR in more detail, the NMR chemical shifts of [^{13}C , ^{15}N]-Hef-IDR were measured at 298, 313, and 349 K. The superposition of the two-dimensional CACO and CON spectra is shown in Fig. 3, *a* and *b*, respectively. Although the ^{13}C chemical shifts have been corrected by the sodium trimethylsilylpropanesulfonate (DSS) peak, the chemical shifts of both $^{13}\text{C}'$ and $^{13}\text{C}^\alpha$ shifted upfield

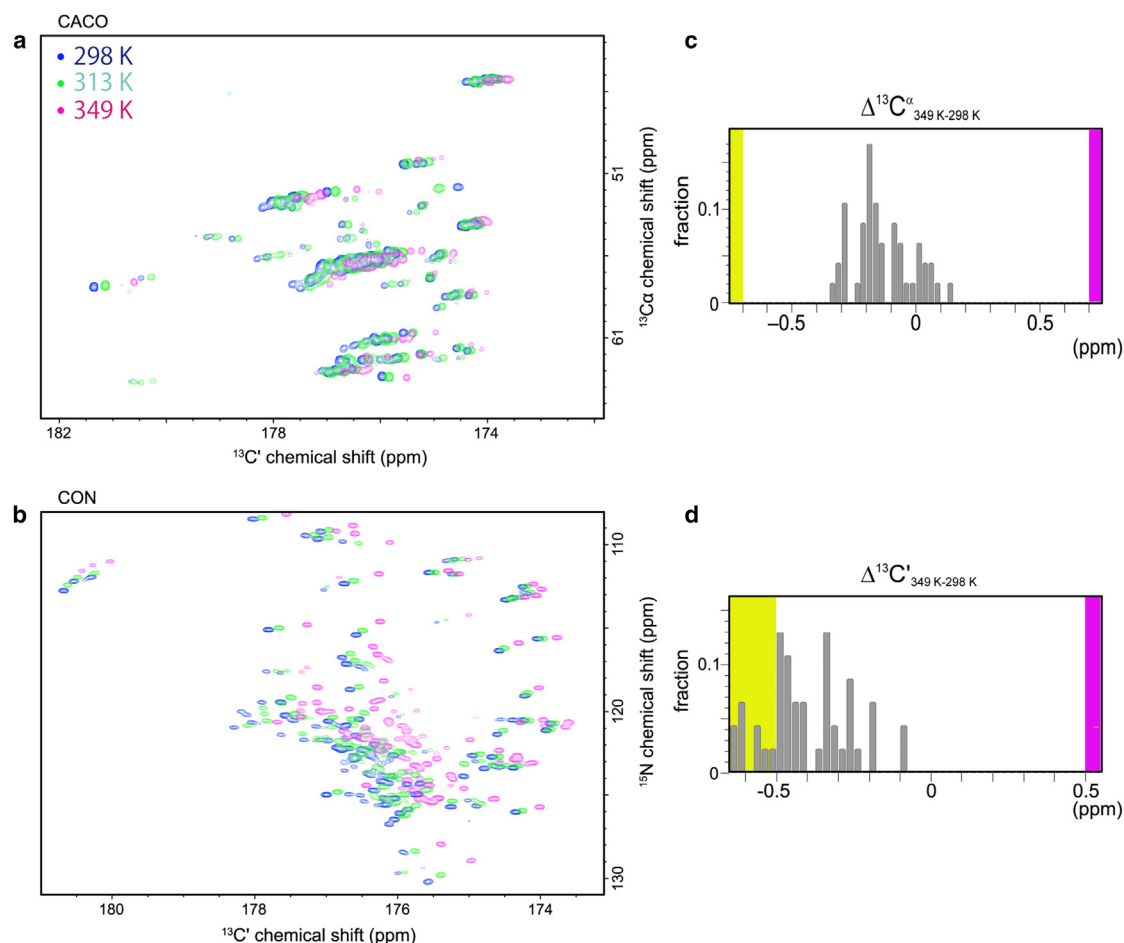


FIGURE 3 Superposition of the CACO (a) and CON (b) spectra measured at 298 (blue), 313 (green), and 349 K (magenta). The $^{13}\text{C}'$ and $^{13}\text{C}^\alpha$ chemical shifts were calibrated using DSS. Histograms of the $^{13}\text{C}^\alpha$ chemical shift differences between 298 and 349 K ($\Delta^{13}\text{C}^\alpha_{343-298\text{K}}$) and $^{13}\text{C}'$ ($\Delta^{13}\text{C}'_{343-298\text{K}}$) are shown in (c) and (d), respectively. Based on the chemical shift index, regions where the chemical shift changes of consecutive residues suggest α helices ($\Delta^{13}\text{C}^\alpha > +0.7$ ppm, $\Delta^{13}\text{C}' > +0.5$ ppm) are shown in purple, whereas regions where those changes suggest β sheets ($\Delta^{13}\text{C}^\alpha < -0.7$ ppm, $\Delta^{13}\text{C}' < -0.5$ ppm) are shown in yellow.

with increasing temperature. It was reported that these chemical shifts in IDPs exhibited temperature dependency (31,32); hence, we focused on the largest differences in the $^{13}\text{C}^\alpha$ and $^{13}\text{C}'$ chemical shifts between 298 and 349 K. Fig. 3, c and d, shows a histogram of the difference in the $^{13}\text{C}^\alpha$ chemical shifts between 298 and 349 K ($\Delta^{13}\text{C}^\alpha_{349-298\text{K}}$) and the $^{13}\text{C}'$ chemical shifts between 298 and 349 K ($\Delta^{13}\text{C}'_{349-298\text{K}}$), respectively. In the formation of the α helix with elevating temperature, it is expected that $\Delta^{13}\text{C}^\alpha_{349-298\text{K}} \geq 0.7$ ppm and $\Delta^{13}\text{C}'_{349-298\text{K}} \geq 0.5$ ppm. In the case of the formation of the β sheet, it is expected that $\Delta^{13}\text{C}^\alpha_{349-298\text{K}} \leq -0.7$ ppm and $\Delta^{13}\text{C}'_{349-298\text{K}} \leq -0.5$ ppm. Therefore, α helix formation was not promoted in the examined temperature range. At elevated temperatures, the exchange rate between different conformations increases, and the observed NMR chemical shift values represent the population-weighted averages of these conformations. Consequently, even if an α helix is transiently populated at high temperatures, the measured

chemical shifts may not exhibit characteristics specific to the α helix due to rapid interconversion with another conformation, such as a β sheet. However, our NMR data at least exclude the dominance of a stable α helix at high temperatures. If the α helix were the predominant and stable conformation, then the $\Delta^{13}\text{C}^\alpha_{349-298\text{K}}$ value would exhibit a more positive shift. Considering the results from CD, SAXS, and NMR, we could deny the possibility of the promotion of the α helix with increasing temperature in Hef-IDR.

The enhancement of hydrophobic interactions at high temperature could be a cause for the present results. Therefore, we performed additional SAXS measurements on the Hef-IDR solution at high NaCl concentration (=1000 mM) at 298 and 363 K: the R_g values are summarized in Table S2. At both temperatures, R_g values were independent of the NaCl concentration within experimental errors, excluding the possibility that the enhancement of hydrophobic interactions at high temperature was the main factor for the present result. The PPII propensity of

Hef-IDR was predicted using PPIIPred (33), and PPII propensity as a function of residue number is shown in Fig. 4. A relatively high PPII propensity was observed near the C-terminal region, supporting the existence of a PPII helix in Hef-IDR. Finally, we concluded that the loss of the PPII helix with increasing temperature is an appropriate interpretation of the temperature-dependent structural change in Hef-IDR.

Temperature dependence of internal dynamics of Hef-IDR

As the scattering cross section of a hydrogen (H) atom is significantly larger than those of other constituent atoms in Hef-IDR, the observed QENS profile is mainly dominated by incoherent dynamic scattering laws. The incoherent dynamic scattering laws indicate that the motion is described by the self-motion of the H atoms. In other words, protein dynamics are detected by H atoms, which are homogeneously distributed throughout the protein structure. Fig. 4 shows dynamics scattering laws ($S(Q, \omega)$) at a mean Q value ($\bar{Q}) = 0.60 \text{ \AA}^{-1}$ at 283, 298, 323, 343, and 363 K using the same model function ($S(Q, \omega)_{\text{mod}}$) adopted in our previous work (10). To extract the reliable information on the internal dynamics, we should calculate the contribution of rigid-body motion, which is given by a combination of translational and rotational diffusions. For this purpose, we performed curve fits to the SAXS profiles using MultiFoXS (34), and the ensemble of four model configurations successfully reproduced the SAXS profiles (solid lines in Fig. 1). The schematic views of the four configurations and their structural parameters are shown in Fig. S6 and Table S3. Notably, the R_g and D_{max} values calculated from the ensemble profiles approximately coincided with those calculated from the SAXS profiles (Table S4). Using the averaged translational and rotational diffusion constants (Table S5) calculated from four model configurations, we analyzed the observed $S(Q, \omega)$ (refer to the supporting material and Table S5). As shown in Fig. 5, the spectra at different temperatures were successfully reproduced using Eq. S3. In the following, we focus on two parameters, $A(Q)$ and Γ , which characterize the internal dynamics of

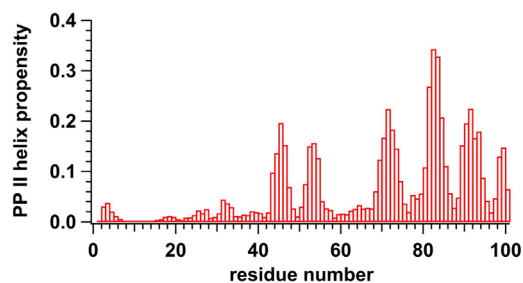


FIGURE 4 PPII propensity of Hef-IDR predicted by PPIIPred

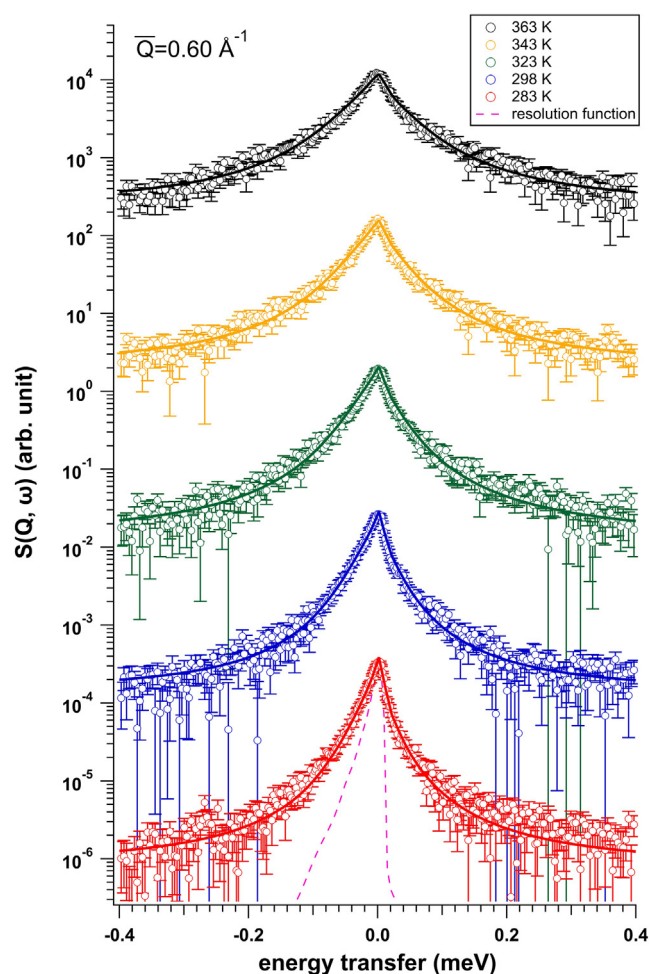


FIGURE 5 The QENS profiles at 283 (red circle), 298 (blue circle), 323 (green circle), 343 (yellow circle), and 363 K (black circle), respectively. The red, blue, green, yellow, and black dotted pink lines correspond to the fit curves and resolution function, respectively.

the Hef-IDR. Nonzero $1-A(Q)$ values at all temperatures indicated the quantitative detection of the internal dynamics of the Hef-IDR (Fig. S7). Because Γ is inversely proportional to the average time constant of the internal dynamics, acceleration of the internal dynamics of the Hef-IDR was observed with increasing temperature (Fig. 6 a). The Q^2 dependence of Γ was fitted using Eq. 3 (35,36):

$$\Gamma = \frac{D_{\text{int}}Q^2}{1 + D_{\text{int}}Q^2\tau_0} \quad (3)$$

where D_{int} and τ_0 correspond to the self-diffusion of the concerned molecule and resident time, respectively. τ_0 is roughly comparable to the timescale of the conformation transition rate (37), and it ranged from 8 to 16 ps, showing the fast rate of conformation change in Hef-IDR. Even when considering an error of $1/\tau_0$, a change in the slope was observed near T_{tra} (Fig. 6 b). The activation energies (E_a) in the temperature ranges below T_{tra} (low-temperature

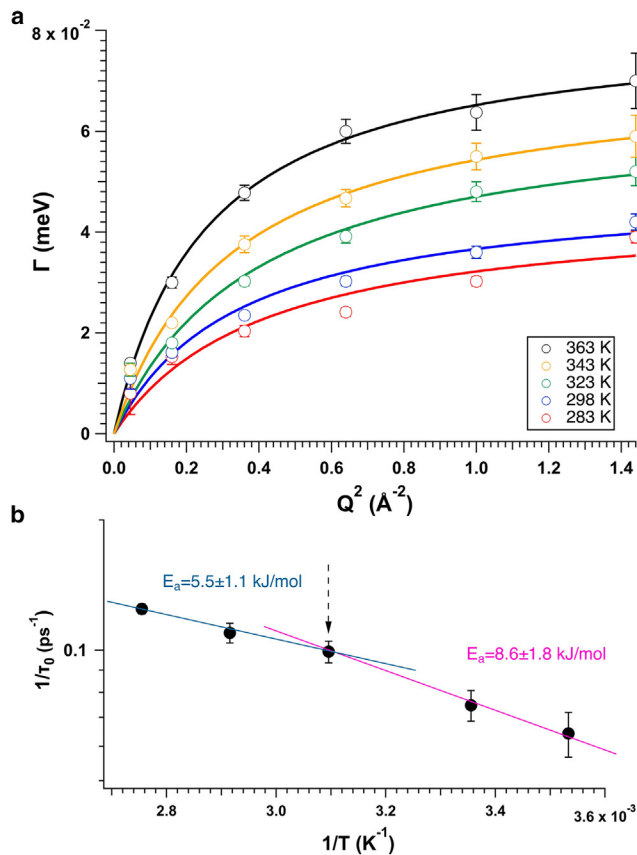


FIGURE 6 (a) Q^2 dependence of the Γ values at 283 (red circles), 298 (blue circles), 323 (green circles), 343 (yellow circles), and 363 K (black circles). Red, blue, green, yellow, and black dotted pink lines correspond to curves fitted with Eq. 3. (b) $1/\tau_0$ as a function of temperature (black circles). The solid green and pink lines correspond to the results of fitting the Arrhenius equation in the high- and low-temperature regions, respectively. The dashed arrow corresponds to T_{tra} .

region) and above T_{tra} (high-temperature region) were analyzed independently using the Arrhenius equation. The E_a values were calculated to be 8.6 ± 1.8 and 5.5 ± 1.1 kJ/mol for low- and high-temperature regions, respectively, showing a transition of internal dynamics at T_{tra} . An inflection temperature was observed at around T_{tra} based on the temperature dependence of D_{int} (Fig. S8).

DISCUSSION

The relaxation time of the network of H-bonds between proteins and water is slower than the average H-bonding of proteins or water because of the dynamical cooperativity between proteins and water (38). As the PPII helix is stabilized by the surrounding water through the formation of a network of H-bonds between the helix and water (39), the network of H-bonds involved in the PPII helix could possess dynamical cooperativity. One of the most famous phenomena coupled with the dynamical cooperativity is the glass transition (40,41). Motivated by the concept of glass transi-

tion, we discuss a plausible mechanism for these results. The acceleration of the internal dynamics (D_{int}) with increasing temperature weakens the dynamical cooperativity between the PPII helix and water. Such weakening of the dynamical cooperativity forces the destabilization of the PPII helix, contributing to the reduction in the fraction of the PPII helix. Then, further weakening of the H-bonding network between the PPII helix and water occurs with further elevation of the temperature, eventually leading to the collapse of the network structure (refer to the left of Fig. 7 a). In the case of the glass transition, this change is detected as an inflection temperature (or T_g), and the E_a above T_g is lower than that below T_g (Fig. 7 b). Consistent with the glass transition, T_{tra} was experimentally detected, and E_a in the high-temperature region was lower than that in the low-temperature region (Fig. 6 b). The PPII helix is extensively observed in various IDPs (33); hence, the dynamical cooperativity between the PPII helix and surrounding water plays a significant role in the temperature-dependent structure of the IDP. Referring to the multistep structural transition of unfolding of cytochrome C (27), we also tried to interpret our results in relation to the local structure of Hef-IDR. A high PPII propensity region (>0.1) was predicted near the C-terminal region and a low PPII propensity one (<0.1) was homogeneously distributed in the amino acid sequence. It is therefore expected that the first stage (high E_a) is predominantly caused by the collapse of the low PPII propensity region with increasing temperature. Above T_{tra} , the high PPII propensity region could start to collapse with a further increase in the temperature. This is related to the second stage (i.e., low E_a).

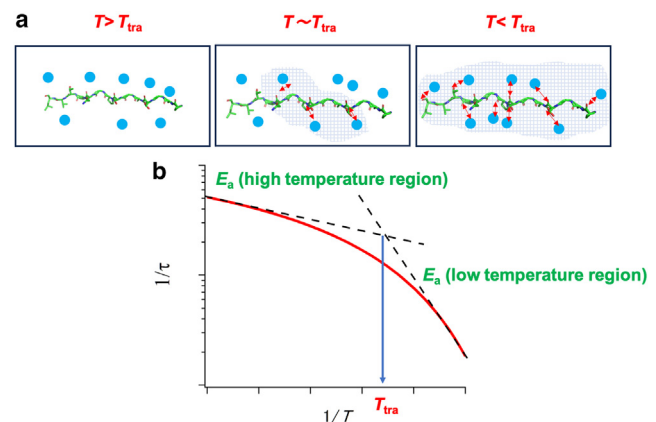


FIGURE 7 (a) Schematic representation of dynamic cooperativity between the PPII helix and water molecules at different temperatures. The green, blue, red, and blue shaded regions correspond to the PPII helix, water molecule, H-bonding between water and PPII helix, and dynamical cooperativity region, respectively. (b) Schematic of $1/\tau_0$ as a function of temperature. The activation energy analyzed in the temperature range higher than T_{tra} was regarded as E_a (high-temperature region), and the activation energy analyzed in the temperature range lower than T_{tra} was regarded as E_a (low-temperature region).

Further detailed analysis of the PPII helix is needed to validate such an expectation.

Finally, we discuss the relationship between the function and the present results. IDP function is regulated mainly by the recognition of binding partners and entropic chain properties. The PPII helix is responsible for molecular recognition (42–44). The growth temperature range of the present Hef-IDR, *T. kodakaraensis*, is 333–373 K (12). Considering both the physiological temperature range of Hef-IDR and the reduction in the content of the PPII helix in that temperature range, entropic chain properties could be involved mainly in the regulation of Hef-IDR function. The entropic chain property of the IDR region of Hef is considered advantageous for configuring the proper orientation of the two globular domains. Therefore, more freedom in the IDR region of Hef may regulate its function.

CONCLUSION

The temperature-dependent structure and dynamics of the Hef-IDR solution were investigated by SAXS, CD, NMR, and QENS. With increasing temperature, both the variation of R_g and $\theta_{222\text{nm}}$ values against temperature were flat. Subsequently, a decrease in these values is observed at around 313–323 K ($=T_{\text{tra}}$). From the dynamic study with the QENS, a change in the E_a was detected at around T_{tra} . Considering the results of the SAXS, CD, and NMR measurements, the decrease in the content of the PPII helix with increasing temperature could be related to the present results. Considering the analogy between the glass transition and the network of H-bonds involved in the PPII helix, we interpreted the present results as follows: the acceleration of internal dynamics weakened the dynamical cooperativity between the PPII helix and water with increasing temperature, leading to a decrease in the content of the PPII helix. With a further increase in temperature, the network of H-bonds between the PPII helix and water collapsed, resulting in the experimental detection of T_{tra} . Namely, the dynamical cooperativity between the PPII helix and surrounding water could be the main contributor to the temperature-dependent structural change in the IDP. The regulation of the internal dynamics enables the desired solution structure of the IDP.

ACKNOWLEDGMENTS

QENS and SANS measurements at J-PARC were performed under proposal nos. 2019L0301 and 2019L0302. The SANS measurements at JRR-3 were performed under proposal nos. 21531 and 22569 and the beamtime for the instrumentation research team. The SAXS measurements at the Photon Factory were performed under proposal nos. 2019G034 and 2021G116. This work was supported by MEXT/JSPS KAKENHI grants (grant nos. JP20K06527 and JP24K09406 to T.O., JP19KK0071 and JP20K06579 to R.I., and JP18H05229, JP18H05534, and JP18H03681 to M. Sugiyama). This work was partially supported by a project for the construction of a basis for advanced materials science and analytical studies through the

innovative use of quantum beams and nuclear sciences at the Institute for Integrated Radiation and Nuclear Science, Kyoto University. This work was partially supported by the deuteration laboratory at the J-PARC MLF. This work was partially supported by the ISHIZUE 2024 of Kyoto University. This study was also partially supported by the Platform Project for Supporting Drug Discovery and Life Science Research (Basis for Supporting Innovative Drug Discovery and Life Science Research [BINDS]) from AMED (JP22ama121001j0001) to M. Sugiyama and proposal no. 4343 to T.O.

AUTHOR CONTRIBUTIONS

Conceptualization, R.I., T.O., M. Sato, and M. Sugiyama; formal analysis, R.I., T.O., H.N., T.T., T.I., T.K., H.I., and Y.K.; investigation, R.I., T.O., H.N., T.T., T.I., T.K., H.I., and Y.K.; writing – original draft preparation, R.I. and T.O.; project administration, R.I., T.O., M. Sato, and M. Sugiyama; funding acquisition, M. Sugiyama; supervision, M. Sato and M. Sugiyama; writing – review & editing, M. Sato and M. Sugiyama.

DECLARATION OF INTERESTS

The authors declare no conflicts of interest associated with this manuscript.

SUPPORTING MATERIAL

Supporting material can be found online at <https://doi.org/10.1016/j.bpj.2024.12.022>.

REFERENCES

1. Wright, P. E., and H. J. Dyson. 1999. Intrinsically unstructured proteins: re-assessing the protein structure-function paradigm. *J. Mol. Biol.* 293:321–331.
2. Uversky, V. N. 2009. Intrinsically disordered proteins and their Environment: effects of strong denaturants, temperature, pH, counter ions, membranes, binding partners, osmolytes, and macromolecular crowding. *Protein J.* 28:305–325.
3. Nettels, D., S. Müller-Späth, ..., B. Schuler. 2009. Single-molecule spectroscopy of the temperature-induced collapse of unfolded proteins. *Proc. Natl. Acad. Sci. USA.* 106:20740–20745.
4. Kjaergaard, M., A. Nørholm, ..., B. B. Kragelund. 2010. Temperature-dependent structural changes in intrinsically disordered proteins: Formation of α -helices or loss of polyproline II? *Proteome Sci.* 19:1555–1564.
5. Wuttke, R., H. Hofmann, ..., B. Schuler. 2014. Temperature-dependent solvation modulates the dimensions of disordered proteins. *Proc. Natl. Acad. Sci. USA.* 111:5213–5218.
6. Jephthah, S., L. Staby, ..., M. Skepö. 2019. Temperature Dependence of Intrinsically Disordered Proteins in Simulations: what are we missing? *J. Chem. Theor. Comput.* 15:2672–2683.
7. Stadler, A. M., L. Stingaciu, ..., D. Richter. 2014. Internal nanosecond dynamics in the intrinsically disordered myelin basic protein. *J. Am. Chem. Soc.* 136:6987–6994.
8. Lin, T.-C., O. Shih, ..., U.-S. Jeng. 2024. Binding structures of SERF1a with NT17-polyQ peptides of huntingtin exon 1 revealed by SECSWAXS, NMR and molecular simulation. *IUCrJ.* 11:849–858.
9. Hassani, A. N., A. M. Stadler, and G. R. Kneller. 2022. Quasi-analytical resolution-correction of elastic neutron scattering from proteins. *J. Chem. Phys.* 157:134103.
10. Inoue, R., T. Oda, ..., M. Sugiyama. 2020. Dynamics of proteins with different molecular structures under solution condition. *Sci. Rep.* 10:21678.

11. Buvalaia, E., M. Kruteva, ..., R. Biehl. 2023. Interchain hydrodynamic interaction and internal friction of polyelectrolytes. *ACS Macro Lett.* 12:1218–1223.
12. Inoue, R., T. Oroguchi, ..., M. Sugiyama. 2023. Internal dynamics of multidomain protein as revealed by an optimized neutron spin echo measurement and all-atom molecular dynamics simulation. *Phys. Rev. Res.* 5:043154.
13. Ishino, S., T. Yamagami, ..., Y. Ishino. 2014. Multiple Interactions of the intrinsically disordered region between the helicase and nuclease domains of the archaeal Hef protein. *J. Biol. Chem.* 289:21627–21639.
14. Shimizu, N., K. Yatabe, ..., N. Igarashi. 2016. Software development for analysis of small-angle x-ray scattering data. *AIP Conf. Proc.* 1741:050017.
15. Petoukhov, M. V., D. Franke, ..., D. I. Svergun. 2012. New developments in the ATSAS program package for small-angle scattering data analysis. *J. Appl. Crystallogr.* 45:342–350.
16. Franke, D., M. V. Petoukhov, ..., D. I. Svergun. 2017. ATSAS 2.8 : a comprehensive data analysis suite for small-angle scattering from macromolecular solutions. *J. Appl. Crystallogr.* 50:1212–1225.
17. Takata, S., J. Suzuki, ..., M. Sugiyama. 2015. The design and q resolution of the small and wide angle neutron scattering instrument (TAIKAN) in J-PARC. *JPS Conf. Proc.* 8:036020.
18. Mayumi, K., L. Geonzon, ..., T. Oda. 2024. Hierarchical structure of soft materials studied at small-angle neutron scattering instrument, SANS-U. *J. Phys. Soc. Jpn.* 93:091007.
19. Bermel, W., I. Bertini, ..., P. R. Vasos. 2005. Complete assignment of heteronuclear protein resonances by protonless NMR spectroscopy. *Angew. Chem., Int. Ed. Engl.* 44:3089–3092.
20. Slad, S., W. Bermel, ..., B. Luy. 2022. Band-selective universal 90° and 180° rotation pulses covering the aliphatic carbon chemical shift range for triple resonance experiments on 1.2 GHz spectrometers. *J. Biomol. NMR.* 76:185–195.
21. Andersson, P., J. Weigelt, and G. Otting. 1998. Spin-state selection filters for the measurement of heteronuclear one-bond coupling constants. *J. Biomol. NMR.* 12:435–441.
22. Lee, W., M. Rahimi, ..., A. Chiu. 2021. POKY: a software suite for multidimensional NMR and 3D structure calculation of biomolecules. *Bioinformatics.* 37:3041–3042.
23. Shibata, K., N. Takahashi, ..., M. Arai. 2015. The Performance of TOF near Backscattering Spectrometer DNA in MLF, J-PARC. *JPS Conf. Proc.* 8:036022.
24. Tominaga, T., M. Sahara, ..., T. Yamada. 2021. Evaluation of sample cell materials for aqueous solutions used in quasi-elastic neutron scattering measurements. *J. Appl. Crystallogr.* 54:1631–1640.
25. Tominaga, T., H. Nakagawa, ..., M. Sugiyama. 2022. Data collection for dilute protein solutions via a neutron backscattering spectrometer. *Life.* 12:675.
26. Guinier, A., G. Fournet, ..., K. L. Yudowitch. 1955. Small-angle Scattering of X-Rays. John Wiley & Sons, New York.
27. Shiu, Y.-J., U.-S. Jeng, ..., S.-H. Lin. 2008. Global and local structural changes of cytochrome c and lysozyme characterized by a multigroup unfolding process. *Biophys. J.* 94:4828–4836.
28. Treviño, M. Á., R. López-Sánchez, ..., D. V. Laurents. 2022. Insight into polyproline II helical bundle stability in an antifreeze protein denatured state. *Biophys. J.* 121:4560–4568.
29. Boze, H., T. Marlin, ..., B. Cabane. 2010. Proline-rich salivary proteins have extended conformations. *Biophys. J.* 99:656–665.
30. Wang, Z., K. W. Plaxco, and D. E. Makarov. 2007. Influence of local and residual structures on the scaling behavior and dimensions of unfolded proteins. *Biopolymers.* 86:321–328.
31. Kjaergaard, M., S. Brander, and F. M. Poulsen. 2011. Random coil chemical shift for intrinsically disordered proteins: effects of temperature and pH. *J. Biomol. NMR.* 49:139–149.
32. Nielsen, J. T., and F. A. A. Mulder. 2018. POTENCI: prediction of temperature, neighbor and pH-corrected chemical shifts for intrinsically disordered proteins. *J. Biomol. NMR.* 70:141–165.
33. Elam, W. A., T. P. Schrank, ..., V. J. Hilser. 2013. Evolutionary conservation of the polyproline II conformation surrounding intrinsically disordered phosphorylation sites. *Proteome Sci.* 22:405–417.
34. Schneidman-Duhovny, D., M. Hammel, ..., A. Sali. 2016. FoXS, FoXSDock and MultiFoXS: Single-state and multi-state structural modeling of proteins and their complexes based on SAXS profiles. *Nucleic Acids Res.* 44:W424–W429.
35. Golub, M., M. Moldenhauer, ..., J. Pieper. 2019. Solution structure and conformational flexibility in the active state of the orange carotenoid protein. Part II: Quasielastic neutron scattering. *J. Phys. Chem. B.* 123:9536–9545.
36. Grimaldo, M., F. Roosen-Runge, ..., F. Schreiber. 2014. Diffusion and dynamics of γ -Globulin in crowded aqueous solutions. *J. Phys. Chem. B.* 118:7203–7209.
37. Kanya, T., T. Kawaguchi, and K. Kaji. 1999. Local dynamics of some bulk polymers above T_g as seen by quasielastic neutron scattering. *Macromolecules.* 32:1672–1678.
38. Schirò, G., Y. Fichou, ..., M. Weik. 2015. Translational diffusion of hydration water correlates with functional motions in folded and intrinsically disordered proteins. *Nat. Commun.* 6:6490.
39. Adzhubei, A. A., M. J. E. Sternberg, and A. A. Makarov. 2013. Polyproline-II helix in proteins: a structure and function. *J. Mol. Biol.* 425:2100–2132.
40. Donth, E. 1982. The size of cooperatively rearranging regions at the glass transition. *J. Non-Cryst. Solids.* 53:325–330.
41. Richter, D., M. Monkenbusch, ..., J. Colmenero. 2005. Neutron Spin Echo in Polymer Systems. Springer Berlin Heidelberg, Berlin, Heidelberg.
42. Williamson, M. P. 1994. The structure and function of proline-rich regions in proteins. *Biochem. J.* 297:249–260.
43. Kay, B. K., M. P. Williamson, and M. Sudol. 2000. The importance of being proline: the interaction of proline-rich motifs in signaling proteins with their cognate domains. *Faseb. J.* 14:231–241.
44. Mompeán, M., J. Oroz, and D. V. Laurents. 2021. Do polyproline II helix associations modulate biomolecular condensates? *FEBS Open Bio.* 11:2390–2399.